INTERNATIONAL JOURNAL FOR NUMERICAL METHODS IN FLUIDS
Int. J. Numer. Meth. Fluids 2007; **53**:1673–1688
Published online 25 October 2006 in Wiley InterScience (www.interscience.wiley.com). DOI: 10.1002/fld.1375

Numerical simulation of turbulent impinging jet on a rotating disk

A. Abdel-Fattah*, †, ‡

Department of Mechanical Power Engineering, Faculty of Engineering, Menoufia University, Shebin El-Kom, Egypt

SUMMARY

The calculations of quasi-three-dimensional momentum equations were carried out to study the influence of wall rotation on the characteristics of an impinging jet. The pressure coefficient, the mean velocity distributions and the components of Reynolds stress are calculated. The flow is assumed to be steady, incompressible and turbulent. The finite volume scheme is used to solve the continuity equation, momentum equations and k–ε model equations. The flow characteristics were studied by varying rotation speed ω for $0 \leqslant \omega \leqslant 167.6$ rad/s, the distance from nozzle to disk (H/d) was (3, 5, 8 and 10) and the Reynolds number Re base on V_J and d was 1.45×10^4. The results showed that, the radial velocity and turbulence intensity increase by increasing the rotation speed and decrease in the impingement zone as nozzle to disk spacing increases. When the centrifugal force increases, the radial normal stresses and shear stresses increase. The location of maximum radial velocity decreases as the local velocity ratio (α) increases. The pressure coefficient depends on the centrifugal force and it decreases as the distance from nozzle to plate increases. In impingement zone and radial wall jet, the spread of flow increases as the angular velocity decreases. The numerical results give good agreement with the experiment data of Minagawa and Obi (*Int. J. of Heat and Fluid Flow* 2004; **25**:759–766). Copyright © 2006 John Wiley & Sons, Ltd.

Received 19 May 2006; Revised 9 August 2006; Accepted 16 August 2006

KEY WORDS: rotating disk; turbulent flow; impinging jet; radial wall jet; velocity distribution; Reynolds stress; RNG model

1. INTRODUCTION

During the manufacture of gas turbines, a detailed knowledge of heat transfer mechanisms is imperative especially in designing highly thermally stressed components such as the turbine disk. A disk cooling scheme which can intensify local heat transfer rates with a relatively low coolant

*Correspondence to: A. Abdel-Fattah, Department of Mechanical Power Engineering, Faculty of Engineering, Menoufia University, Shebin El-Kom, Egypt.
†E-mail: ashourabdelfatah@yahoo.com
‡Associate Professor.

flow rate consists of squirting a coolant jet at the rotating disk. This scheme is currently applied in the space shuttle main engine turbo pumps. In addition to their application in turbo machinery, the disk jet flows have a great variety of general applications.

A number of investigations have been done with respect to the impinging jet on a stationary wall; some work was experimental and others were numerical. There are a number of experimental measurements by Cooper *et al.* [1], Baughn and Shimzv [2], Lytle and Webb [3], Baughn *et al.* [4] and Knowles and Myszko [5], in their study, they measured the mean velocity and turbulence intensities for a single circular jet impinging onto a flat ground board. Baydar [6] measured the pressure and axial velocity for the flow in two dimensions in r–z axes of single and double impinging jet. Some numerical investigations were reported by Wolfshtein [7], Amano and Bradt [8]. Poh *et al.* [9] studied the flow and heat transfer characteristics of a single axisymmetric semi-confined impinging laminar jet. Salmanzadeh *et al.* [10] used $v^2 - f$ model to study the flow and thermal fields in an axisymmetric, fully developed, turbulent, impinging jet on a flat plate. The heat transfer from an annular laminar jet was studied numerically by Chattopadhyay [11]. There has been little work on the impinging jet on a rotating disk. Brodersen *et al.* [12, 13] performed measurements of mean velocity and turbulence intensity in the flow field resulting from the interaction between an impinging jet on a rotating disk at a distance from the rotation axis, and the turbulence boundary layer on the rotating disk. Itoh and Okada [14] conducted detailed measurements on a turbulent wall jet developed on a rotating disk and showed that the turbulence structure in the boundary layer deviated from the equilibrium state as the disk rotation speed increases. Minagawa and Obi [15] studied experimentally the impinging jet on a rotating disk. Their results showed the effect of disk rotation and the centrifugal force on the characteristics of steady, axisymmetric and turbulent impinging jet on a rotating disk. Kubo and Gouldin [16] used the standard k–ε model for calculating the characteristics of the turbulent swirling flow. The impeller shroud to casing leakage flow simulations in the space shuttle main engine high-pressure fuel pump was studied numerically by Sinder and published by Yong [17]. He used k–ε and Boussinesq approximations to obtain the Reynolds stresses. Development of a hybrid k–ε turbulence model for swirling recirculating flow under moderate to strong swirl intensities was investigated by Chang and Chen [18]. Chuang and Nieh [19] studied the characteristics of flow of square twin-jet without cross flow. They calculated the turbulent viscosity by solving the standard k–ε turbulence model. The prediction of a turbulent plane jet in crass flow was investigated by Kalita *et al.* [20]. They used k–ε and Boussinesq approximations to calculate the turbulence viscosity and the Reynolds stresses.

The standard k–ε model was used to study the turbulent slot jet impinging on a semi-cylindrical convex surface by Hwang and Yang [21]. The comparison of Yang-Shih and standard k–ε turbulence model was studied by El-Gabry and Kaminski [22]. They showed that the standard k–ε turbulence model is better at a high Reynolds number and it is not possible to conclude that one turbulence model is more accurate than another. The turbulent fluid flow and heat transfer characteristics of heated rectangular plates such as fins mounted over a surface were investigated numerically by Velayati and Yaghoubi [23]. They calculated the turbulence viscosity by solving an RNG based k–ε turbulence model.

In this present numerical study, the effect of disk rotation, the centrifugal force and the distance between the nozzle and the disk on the characteristics of a steady, axisymmetric and turbulent impinging jet on a rotating disk are studied. These characteristics are pressure coefficient, mean radial velocity, maximum radial velocity, the location of maximum radial velocity and normal and shear components of the Reynolds stress. For comparison between this work and measurements data [15], the centrifugal force is determined by the ratio of the circumferential and radial

DOI: 10.1002/fld

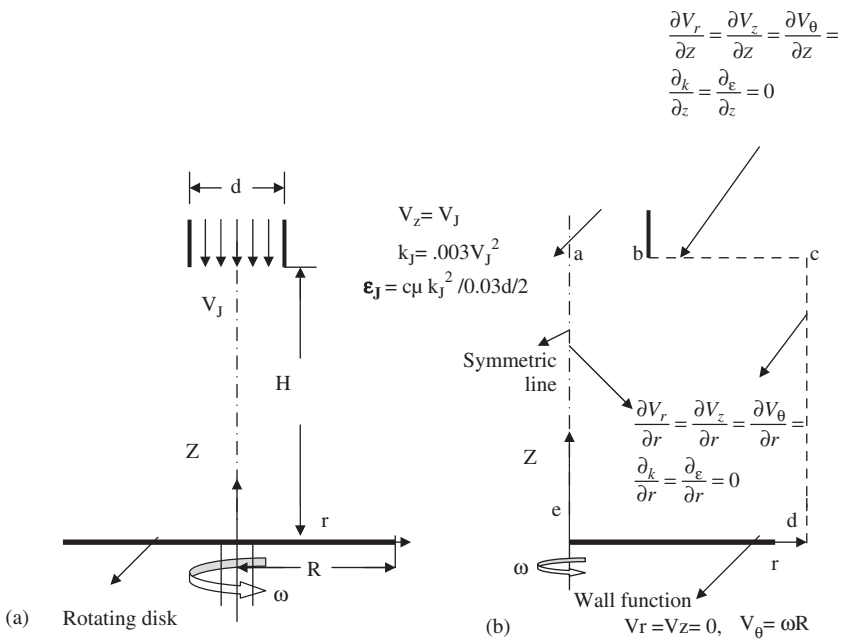

Figure 1. (a) Flow configuration and coordinate system of the problem; and (b) boundary conditions for computation.

velocity components (α), i.e. $\alpha = V_\theta / V_r$, where the V_θ on the wall is $1/r$, a local α equal to $r\omega$ considering that the decrease of radial velocity component V_r is velocity ratio which can be written as

$$\alpha = \frac{r\varpi}{V_J/(r/d)} = \frac{r^2\varpi}{V_J d}$$

2. GOVERNING EQUATIONS

The configuration to be studied is shown in Figure 1(a). Calculation of a turbulent impinging jet on a rotating disk requires the simultaneous solution of the governing equations. The jet flow on the rotating disk with constant angular velocity is quasi-three dimensional, incompressible and turbulent. Based on the characteristic scales of d and V_J, the dimensionless variables are defined as follows:

$$Z = \frac{\overline{Z}}{d}, \quad r = \frac{\overline{r}}{d}, \quad V_r = \frac{\overline{V}_r}{V_J}, \quad V_z = \frac{\overline{V}_z}{V_J}, \quad V_\theta = \frac{\overline{V}_\theta}{\varpi R}, \quad P = \frac{\overline{p}}{\rho V_J^2}$$

where the over bar represents the dimensional quantities. According to the above assumptions and dimensionless variables, the dimensionless governing equations are expressed as the following

DOI: 10.1002/fld

equations:

Continuity equation:

$$\frac{1}{r}\left(\frac{\partial r V_z}{\partial_z}+\frac{\partial r V_r}{\partial r}\right)=0 \tag{1}$$

Axial momentum equation:

$$V_z\frac{\partial V_z}{\partial z}+V_r\frac{\partial V_z}{\partial r}=-\frac{\partial p}{\partial z}+\frac{\partial}{\partial z}\left[\left(\frac{1}{Re}+\frac{1}{Re_t}\right)\frac{\partial V_z}{\partial z}\right]+\frac{1}{r}\frac{\partial}{\partial r}\left[r\left(\frac{1}{Re}+\frac{1}{Re_t}\right)\frac{\partial V_z}{\partial r}\right]$$
$$+\frac{\partial}{\partial z}\left(\frac{1}{Re_t}\frac{\partial V_z}{\partial z}\right)+\frac{1}{r}\frac{\partial}{\partial r}\left(\frac{r}{Re_t}\frac{\partial V_r}{\partial z}\right) \tag{2}$$

Radial momentum equation:

$$V_z\frac{\partial V_r}{\partial z}+V_r\frac{\partial V_r}{\partial r}-\frac{\omega^2R^2}{V_j^2}\frac{V_\theta^2}{r}=-\frac{\partial p}{\partial r}+\frac{\partial}{\partial z}\left[\left(\frac{1}{Re}+\frac{1}{Re_t}\right)\frac{\partial V_r}{\partial z}\right]+\frac{1}{r}\frac{\partial}{\partial r}\left[r\left(\frac{1}{Re}+\frac{1}{Re_t}\right)\frac{\partial V_r}{\partial r}\right]$$
$$+\frac{\partial}{\partial z}\left(\frac{1}{Re_t}\frac{\partial V_z}{\partial r}\right)+\frac{1}{r}\frac{\partial}{\partial r}\left(\frac{r}{Re_t}\frac{\partial V_r}{\partial r}\right)-\frac{2V_r}{Re_tr^2} \tag{3}$$

Tangential momentum:

$$V_z\frac{\partial V_\theta}{\partial z}+V_r\frac{\partial V_\theta}{\partial r}+\frac{V_rV_\theta}{r}=\frac{\partial}{\partial z}\left[\left(\frac{1}{Re}+\frac{1}{Re_t}\right)\frac{\partial V_\theta}{\partial z}\right]+\frac{1}{r}\frac{\partial}{\partial r}\left[r\left(\frac{1}{Re}+\frac{1}{Re_t}\right)\frac{\partial V_\theta}{\partial r}\right]$$
$$+\frac{1}{r^2}\frac{\partial}{\partial r}\left[\left(\frac{r}{Re}+\frac{r}{Re_t}\right)V_\theta\right] \tag{4}$$

The turbulent stresses are modelled as:

$$\overline{-v_z'v_r'}-=\frac{1}{Re_t}\left(\frac{\partial V_z}{\partial r}+\frac{\partial V_r}{\partial z}\right),\quad \overline{-v_r'^2}=\frac{2}{Re_t}\left(\frac{\partial V_r}{\partial r}\right)-\frac{2}{3}k$$
$$\overline{-v_z'^2}=\frac{2}{Re_t}\left(\frac{\partial V_z}{\partial z}\right)-\frac{2}{3}k,\quad \overline{-v_z'}v_\theta'=\frac{1}{Re_t}\left(\frac{\partial V_\theta}{\partial z}\right)$$
$$\overline{-v_\theta'^2}=\frac{2}{Re_t}\left(\frac{V_\theta}{r}\right)-\frac{2}{3}k\quad\text{and}\quad\overline{-v_\theta'v_r'}=\frac{r}{Re_t}\frac{\partial}{\partial r}\left(\frac{V_\theta}{r}\right)$$

where

$$\mu_t=c_\mu\frac{\rho k^2}{\varepsilon}$$

DOI: 10.1002/fld

Here μ_t is the eddy viscosity, c_μ is a model constant, k is the turbulent kinetic energy, and ε is the dissipation rate of the turbulent kinetic energy. The transport equations for turbulent kinetic energy and its dissipation are given by

$$V_r\frac{\partial k}{\partial r}+V_z\frac{\partial k}{\partial z}=\frac{1}{r}\frac{\partial}{\partial r}\left[r\left(\frac{1}{Re}+\frac{1}{\sigma_k Re_t}\right)\frac{\partial k}{\partial r}\right]+\frac{\partial}{\partial z}\left[\left(\frac{1}{Re}+\frac{1}{\sigma_k Re_t}\right)\frac{\partial k}{\partial z}\right]+G-\varepsilon \tag{5}$$

$$V_r\frac{\partial \varepsilon}{\partial r}+V_z\frac{\partial \varepsilon}{\partial z}=\frac{1}{r}\frac{\partial}{\partial r}\left[r\left(\frac{1}{Re}+\frac{1}{\sigma_\varepsilon Re_t}\right)\frac{\partial \varepsilon}{\partial r}\right]+\frac{\partial}{\partial z}\left[\left(\frac{1}{Re}+\frac{1}{\sigma_\varepsilon Re_t}\right)\frac{\partial \varepsilon}{\partial z}\right]+c_1\frac{\varepsilon}{k}G-c_2\frac{\varepsilon^2}{k} \tag{6}$$

where G is the rate of production of k and is given by

$$G=\frac{1}{Re_t}\left[\left(\frac{\partial V_r}{\partial z}+\frac{\partial V_z}{\partial r}\right)^2+2\left(\frac{\partial V_r}{\partial r}\right)^2+2\left(\frac{V_r}{r}\right)^2+2\left(\frac{\partial V_z}{\partial z}\right)^2+\left(r\frac{\partial}{\partial r}\left(\frac{V_\theta}{r}\right)\right)^2+\left(\frac{\partial V_\theta}{\partial z}\right)^2\right]$$

The values of the model constants are taken as:

$$c_\mu=0.09,\quad c_1=1.44,\quad c_2=1.92,\quad \sigma_k=1\quad\text{and}\quad \sigma_\varepsilon=1.3$$

The renormalization group dissipation equation and constant values are proposed by Velayati and Yoghoubi [23]

$$V_r\frac{\partial \varepsilon}{\partial r}+V_z\frac{\partial \varepsilon}{\partial z}=\frac{1}{r}\frac{\partial}{\partial r}\left[r\left(\frac{1}{Re}+\frac{1}{\sigma_\varepsilon Re_t}\right)\frac{\partial \varepsilon}{\partial r}\right]+\frac{\partial}{\partial z}\left[\left(\frac{1}{Re}+\frac{1}{\sigma_\varepsilon Re_t}\right)\frac{\partial \varepsilon}{\partial z}\right]+\frac{\varepsilon}{k}\left(c_1-\frac{\eta(1-(\eta/\eta_0))}{1+\beta\eta^3}\right)G-c_2\frac{\varepsilon^2}{k} \tag{7}$$

where $\eta=\sqrt{c_\mu^{-1}(G/\rho\varepsilon)}$.

The values of the model constants are taken as:

$$c_\mu=0.085,\quad c_1=1.44,\quad c_2=1.68,\quad \sigma_k=0.719,\quad \sigma_\varepsilon=0.719,\quad \eta_0=4.38\quad\text{and}\quad \beta=0.012$$

The computational domain boundaries are shown in Figure 1(b).

The boundary conditions for the above set of governing equations are as follows:

(a) Inlet boundary (a–b).
The uniform velocity, and turbulent kinetic energy dissipation rate are:

$$k_J=0.003V_J^2,\quad \varepsilon_J=\frac{c_\mu k_J^{1.5}}{0.03d/2}\quad\text{and}\quad V_z=V_J$$

(b) at (b–c)
A zero gradient condition is used $\partial\phi/\partial z=0$, where $\Phi=V_r$, V_z, V_θ, k and ε

(c) Exit boundary (c–d) and symmetric line (e–a).
A zero gradient condition is employed across the outlet boundary. Although this boundary condition is strictly valid only when flow is fully developed, it is also permissible at a

DOI: 10.1002/fld

sufficient downstream distance from the region of interest.

$$\partial\phi/\partial r = 0 \quad \text{where } \phi = V_r, V_z, V_\theta, k \text{ and } \varepsilon$$

(d) at walls (c–e).

The condition at a solid wall are imposed $V_r = V_z = 0$ and $V_\theta = \omega r$. In the standard k–ε model, the velocity at the grids adjacent to the wall are specified by wall function. The wall function is suggested by Launder and Spalding [24].

3. SOLUTION PROCEDURE

The mathematical models described above consist of a set of differential equations subject to appropriate boundary conditions. To provide the algebraic form of the governing equations, a fully staggered grid system was adopted for the velocity components and the scalar variables and these equations were discretized using a control volume finite difference methods (CVFDM). The numerical solution in the present work is accomplished by using semi-implicit method for pressure linked equation (SIMPLE) utilized by Patankar [25]. In this algorithm the velocity components V_z is calculated at the north and south faces of the main control volumes from the solution of the axial momentum equation. Similarly, the velocity component V_r at east and west faces and the component V_θ at centre of the main control volume are obtained. Then the pressure correction equation is solved, then the velocity and the pressure fields are corrected. To complete an iteration, the turbulent kinetic energy and energy dissipation rate are solved successively. The discretization equation was solved by the line-by-line procedure, which is a combination of Gauss–Seidel and tridiagonal matrix algorithm (TDMA) in the stream wise direction. The TDMA was used to solve a set of discretization equation in the cross-equations in the cross-stream direction. Relaxation factors were employed to promote smooth convergence of the discretized equations. The relaxation factors were 0.75, 0.75, 0. 5, 0.5, 0.1 and 0.1 for V_z, V_r, V_θ, p', k and ε, respectively. The turbulent viscosity was under relaxed at a value of 0.1. The converged criterion in this study was based on the successive changes in variables. All field variables were monitored, and the following condition was used to declare convergence:

$$\text{MAX}\left|\frac{\phi_{i,j}^n - \phi_{i,j}^{n-1}}{\phi_{i,j}^n}\right| \leqslant 10^{-4} \tag{8}$$

In addition, the ratio of the difference between the inlet mass flow rate and the outlet mass flow rate to the inlet mass flow rate was also examined. Convergence was declared if the relative mass imbalance was less than 10^{-3} and Equation (8) were satisfied simultaneously. To verify the algorithm, numerical tests were performed to ensure that the solution were grid algorithm.

The grid points are not distributed uniformly over the computational domain. The grid points have a greater density near the symmetric line in the radial direction and near the plate in the normal direction. A 105×85 grid points with a power 1.03×1.03 were placed in the computational domain. Results at a grid independent study is shown in Figure 2(a). The effect of the turbulence models on the normal component of the Reynolds stresses v_r' is shown in Figure 2(b).

DOI: 10.1002/fld

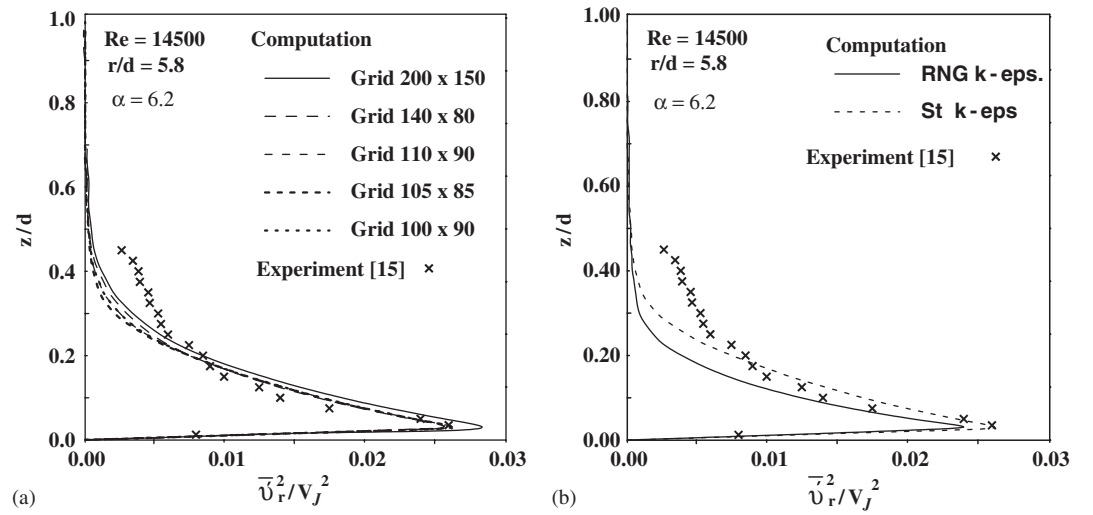

Figure 2. (a) Effect of grid refinement on normal component of Reynolds stress (v_r'); and (b) effect of turbulence model on component of Reynolds stress (v_r').

4. RESULTS AND DISCUSSION

4.1. The mean flow vector fields

Figure 3(a)–(c) shows the mean velocity vectors fields at $Re = 14\,500$, $H/d = 5$ for different values of angular velocity disk. In each case the flow pattern is apparent. The jet flow issues from the nozzle and it spreads in the radial direction and it decelerates until it impacts with the disk, then it converts into the radial direction. The spreading of flow increases by increasing the radial distance for all cases. When the angular velocity increases , the intensity of the flow increases. This is because the circumference velocity effects on the radial velocity of the flow. When the nozzle to disk spacing increases, the spreading of the jet increases at constant angular velocity for the disk, see Figures 3(c) and (d).

4.2. The influence of angular velocity disk on the radial velocity

Figure 4 shows the radial velocity (V_r) at a constant distance from wall ($z/d = 0.032$) for different values of angular velocity disk (ω). From this figure, it is seen that, the radial velocity vanishes at the disk centre, where $r = 0$ and rapidly increases to its maximum, before gradually reducing due to the entrainment of the surrounding fluid and spreading in the circumferential direction. Also it can be seen that, the influence of the rotating disk appears in a region away from disk centre. The velocity increases by increasing the disk angular velocity. This increment in the velocity becomes more obvious at a higher rotational speed when the decrease in this velocity becomes less significant. The influence of disk rotation on the turbulent intensity v_r'/V_j of the radial velocity (i.e. RMS, which calculated with $v_r' = \sqrt{\overline{V_r^2}}$) is shown in Figure 4(b). It can be seen that it is also a minimum at the disk centre and reaches its maximum before diminishing further downstream. Also, the effect of disk rotation in the region is located away from the disk centre. This is because

DOI: 10.1002/fld

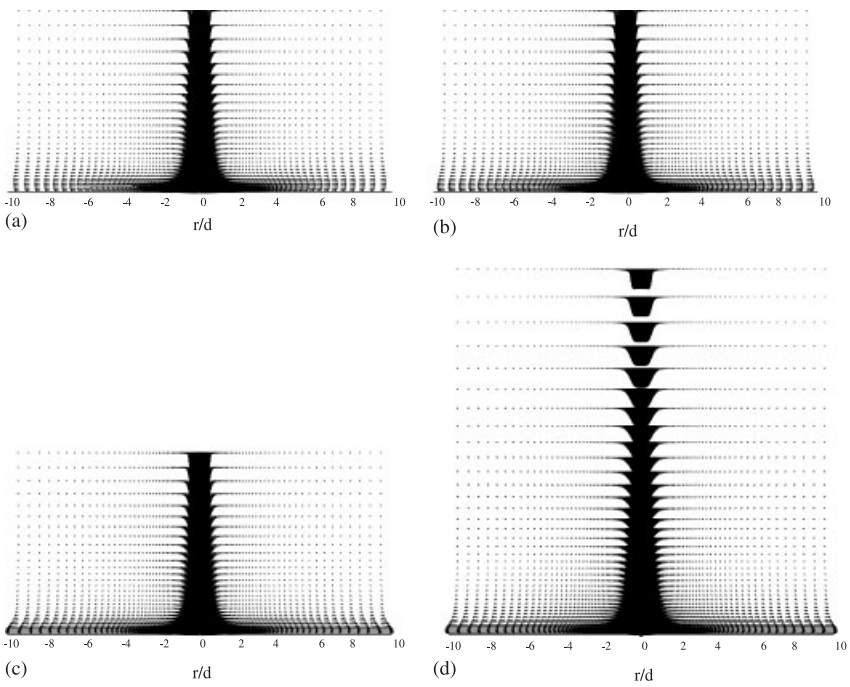

Figure 3. Mean velocity vector field: (a) $H/d = 5$, $Re = 14\,500$, $\omega = 0.0$ rad/s; (b) $H/d = 5$, $Re = 14\,500$, $\omega = 52.4$rad/s; (c) $H/d = 5$, $Re = 14\,500$, $\omega = 157.1$rad/s; and (d) $H/d = 10$, $Re = 14\,500$, $\omega = 157.1$rad/s.

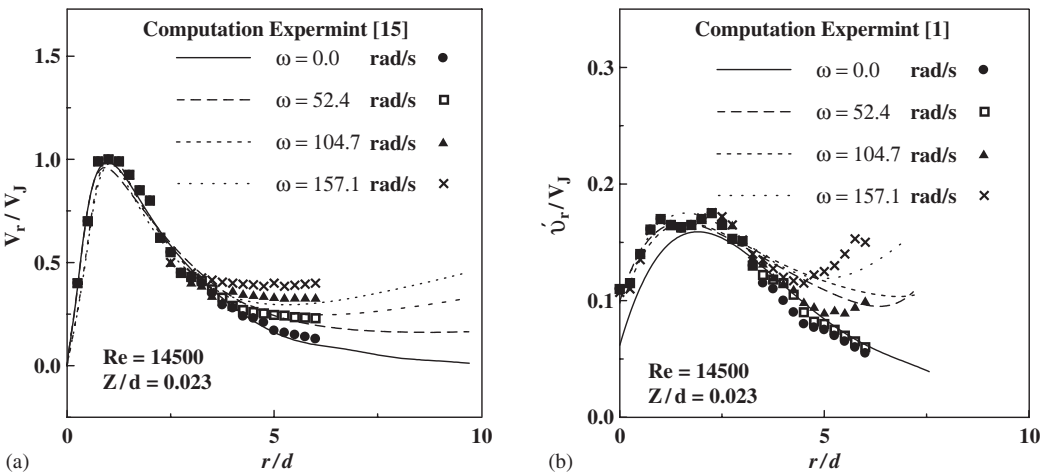

Figure 4. (a) Variation of dimensionless radial velocity with angular velocity disk; and (b) variation of dimensionless turbulence intensity with angular velocity disk.

DOI: 10.1002/fld

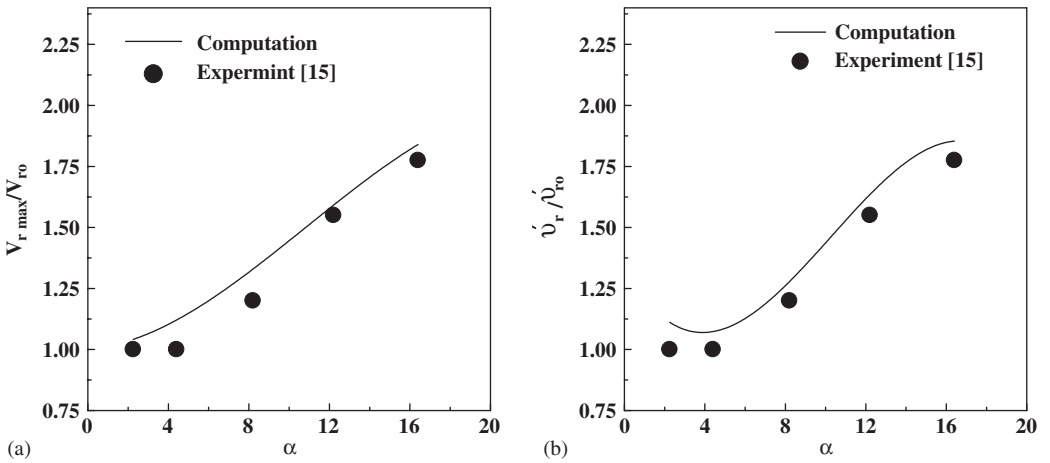

Figure 5. (a) Variation of $V_{r\,\max}/V_{r0}$ as a function of parameter α; and (b) variation of v'_r/v'_{r0} at the location of $V_{r\,\max}$ as a function of parameter α.

the centrifugal force increases with rising circumferential velocity component which is realized by increasing either the rotational speed or the disk radius.

Figure 5 shows the effect of the centrifugal force, on the maximum radial velocity in Figure 5(a), and turbulent intensity Figure 5(b), where v'_r is calculated at the same position as $V_{r\,\max}$, they are normalized by the values calculated without disk rotation at the same radial location of V_{r0} and v'_{r0}, respectively. From this figure, it can be seen that, the effect of centrifugal force becomes obvious for $4.7 \leqslant \alpha$ where $V_{r\,\max}$ starts to increase proportionally to α, while the turbulent intensity begins to increase from $\alpha \sim 2.5$, see Figure 3(b). This is because the parameter α is determined by the ratio of the circumferential and radial velocity components. In the first zone which is the impinging zone, V_r increases and V_θ also increases, then the parameter α depends on both values, hence the effect is not clear. But in the wall jet region, V_r decreases while the V_θ increases, then the parameter α increases, thus the ratio $V_{r\,\max}/V_{r0}$ and v'_r/v'_{r0} increases.

Figure 6 shows the ratio between the location of $V_{r\,\max}(\delta)$ and the location of V_{r0} without disk rotation (δ_0) as a function of the parameter α. It can be seen that, the location (δ/δ_0) changes toward the wall. The shift of location is small at low values of $\alpha \leqslant 4.7$, and this shift becomes evident at $4.7 \leqslant \alpha \leqslant 9.2$, while the shift becomes less significant at $10 \leqslant \alpha$. This is because the effect of centrifugal force is weak in the impingement zone, but the effect of this force becomes bigger in the wall jet region. This depends on the calculation of α. In the first region, the effect of centrifugal force cannot appear. This is because the influence of impingement would become more obvious, resulting in strong flow acceleration in the radial direction. As a consequence, the decay of V_r would be postponed and the relative influence of V_θ might become weaker for the same value of α as in the present case. The centrifugal force becomes stronger in the intermediate region, (the second region). This is because the circumferential velocity increases, and the radial velocity decrease, resulting in the increase of radial direction r. Also, it can be seen that the influence of this force (centrifugal force) becomes weak in the extreme region.

DOI: 10.1002/fld

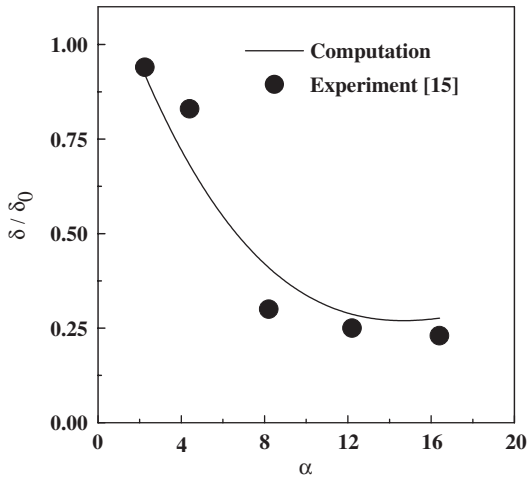

Figure 6. Location of $V_{r\max}/V_{r0}$ as a function of parameter α.

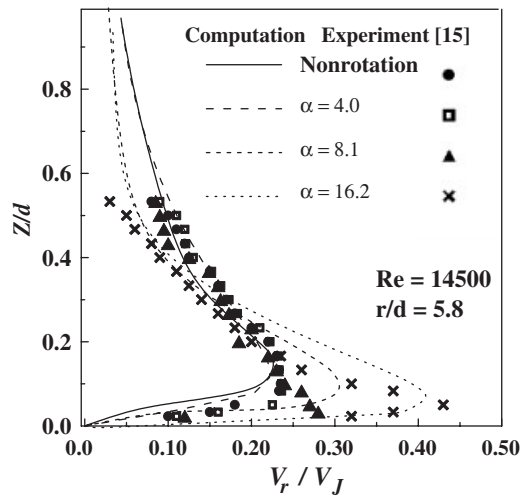

Figure 7. Variation of radial velocity as a function of z/d at different values of α.

4.3. Effect of centrifugal force on mean velocity

Figure 7 shows the radial component velocity V_r as function of vertical distance z/d at $r/d = 5.8$ and for different values of α. From this figure, it is noted that, the profile of this velocity increases to a maximum value and decreases by increasing the vertical distance. When the disk rotates, the location of maximum velocity shifts toward the wall. For $\alpha = 16.2$, the maximum radial velocity reaches nearly twice as much of that of the stationary case, i.e. the acceleration of the centrifugal force to control the wall jet.

DOI: 10.1002/fld

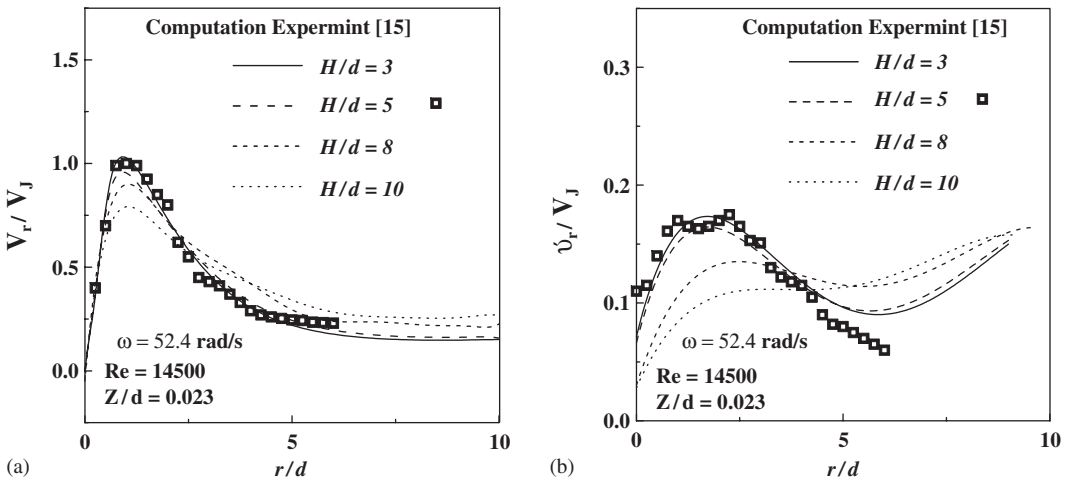

Figure 8. (a) Variation of dimensionless radial velocity with nozzle to disk spacing; and (b) variation dimensionless turbulent radial velocity with nozzle to disk spacing.

4.4. The influence of nozzle to disk spacing on the radial velocity

Figures 8(a) and (b) shows the effect of nozzle to disk spacing on the radial velocity (a) and turbulent intensity (b) at ($z/d = 0.032$) as a function of radial distance. Starting from the stagnation point, the radial velocity along the wall increases with radial distance under the influence of a favourable pressure gradient then decreases due to viscous dissipation. Also, it can be seen that, when the nozzle to disk spacing increases this velocity decreases. Thus, the impingement region increases as the nozzle to plate spacing increases. The turbulence intensity v_r' of this velocity at the same condition is shown in Figure 8(b). From this figure, it is noted that the turbulence intensity increases by increasing H/d.

4.5. Effect of centrifugal force on Reynolds stresses

Figure 9(a)–(c) represents selection of the three normal components of the Reynolds stresses $\overline{v}_r'^2$, $\overline{v}_\theta'^2$, $\overline{v}_z'^2$ for different values of parameter α. From this figure, it can be seen that, the influence of disk rotation on all three components is obvious. The increase in α results in the generation of turbulence. The increase in $\overline{v}_r'^2$ at higher testing value ($\alpha = 16.2$) is almost five times the result without disk rotation. The increase in $\overline{v}_\theta'^2$ however, is much more obvious, yielding the difference of more than an order of magnitude relative to the result without rotation. The reason is that in the flow without rotation, the production of $\overline{v}_\theta'^2$ is zero while the disk rotation produces a shear rate of $\partial V_\theta/\partial Z$. For normal component $\overline{v}_z'^2$ shown in Figure 9(c), it is found that, the value of this component for higher testing value ($\alpha = 16.2$) is very less comparing it with the cases in Figure 9(a) and (b).

4.6. Effect of centrifugal force on shear stress components

The shear stress components $\overline{v_r' v_z'}$ and $\overline{v_r' v_\theta'}$ are shown in Figure 10(a) and (b). The influence of disk rotation is weak since the production of this component does not contain the direct effect,

DOI: 10.1002/fld

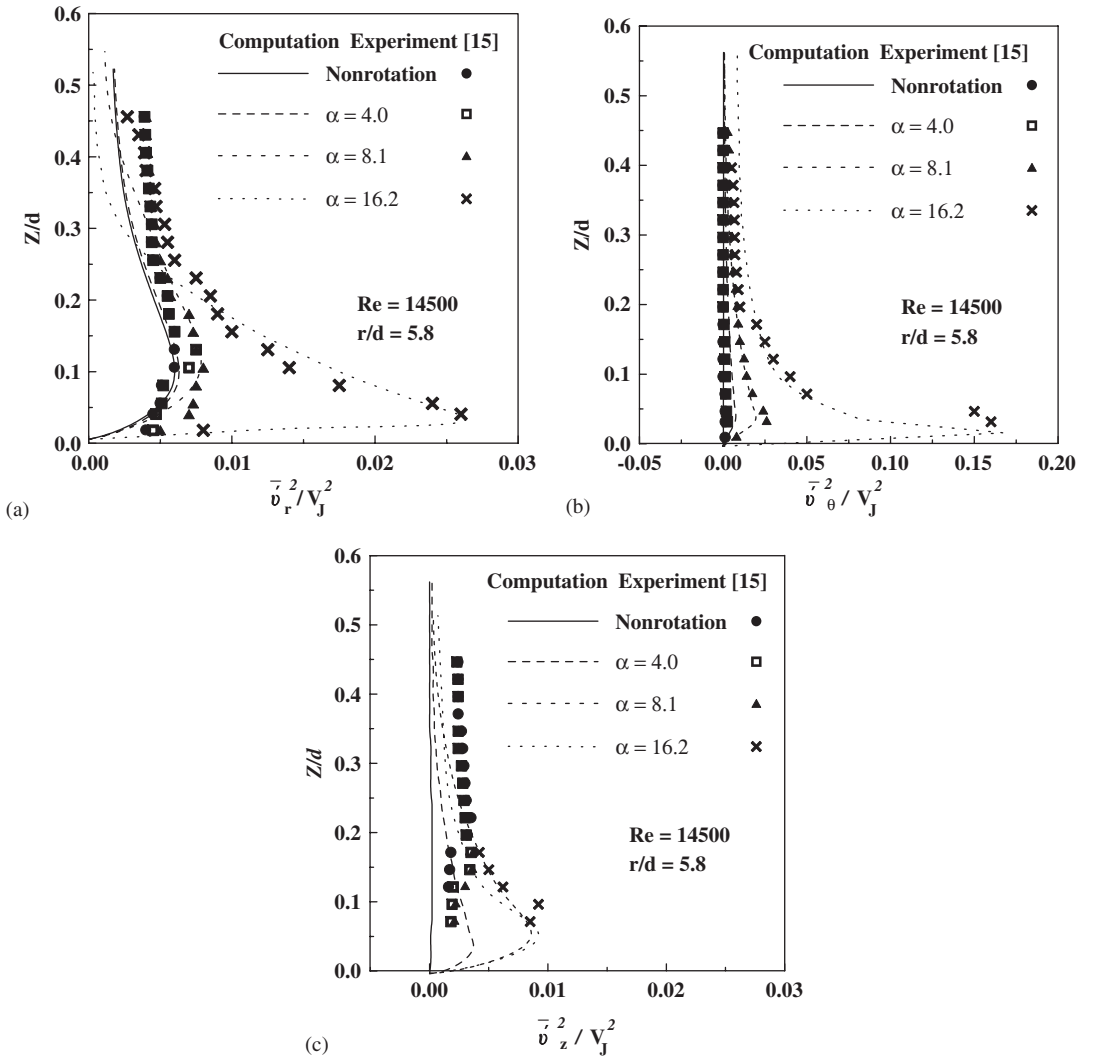

Figure 9. Normal components of Reynolds stress.

but still recognized in the sense that the increasing α provides larger turbulence. With increasing α, the profiles of these components gradually deviate and at $\alpha = 16.2$, the profile is qualitatively different. The $\overline{v_r' v_\theta'}$ is absent when the disk is stationary, and therefore, should reflect more directly the influence of disk rotation. Extremely large values are observed adjacent the wall when the disk rotation is applied; see Figure 10(a).

4.7. Pressure coefficient

Figure 11(a) shows the static wall pressure as a function of radial distance for different values of angular velocity disk at $Re = 1.45 \times 10^4$. It can be seen, from this figure, that the distribution

DOI: 10.1002/fld

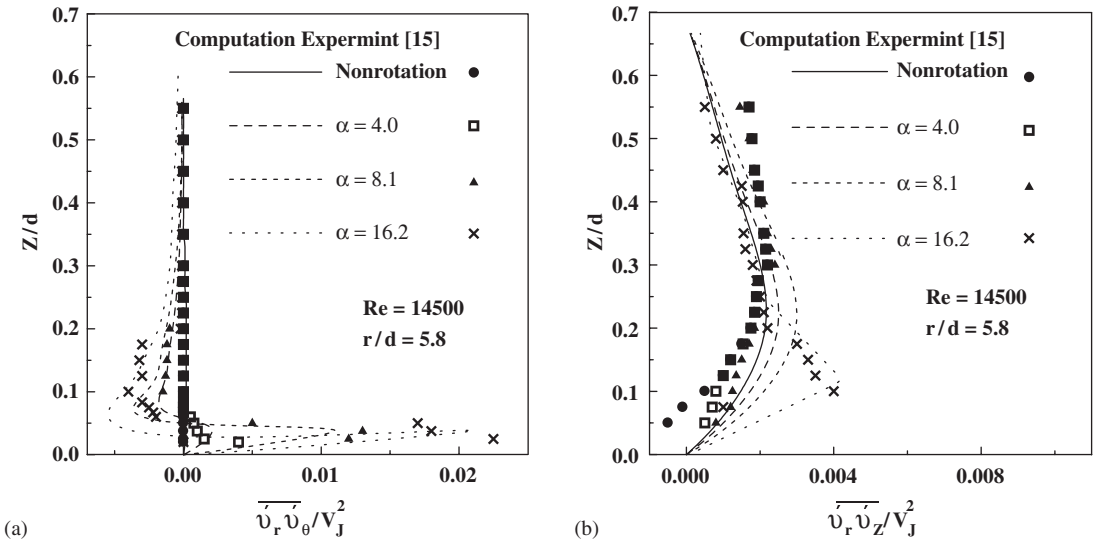

Figure 10. (a) $\overline{v_r'}\overline{v_\theta'}$ component of Reynolds stress; and (b) $\overline{v_r'}\overline{v_z'}$ component of Reynolds stress.

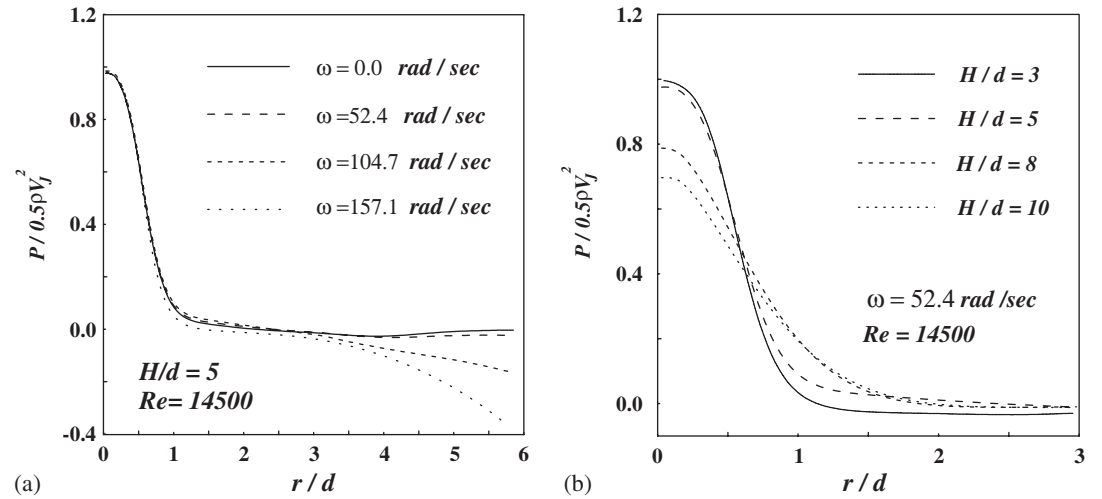

Figure 11. (a) Wall pressure coefficient with angular velocity disk; and (b) wall pressure coefficient with nozzle to disk spacing.

of pressure coefficient is maximum at stagnation point and decreases to zero value as the radial distance increases. This is because the presence of the impinging plate gives rise to the deceleration and deflection of the flow, accordingly the pressure increases at stagnation point, and it decreases along the radial distance. Thus, the kinetic energy increases in the impingement zone. When the

DOI: 10.1002/fld

disk angular velocity increases, the effect of rotating disk appears in a region away from disk centre. Thus, the pressure decreases in the intermediate region and extreme region. This is because, the radial velocity increases as the circumferential velocity disk increases. This pressure decreases as the nozzle to disk spacing increases, see Figure 11(b). This is because, the spread of the jet in the axial direction increases and the kinetic energy which converts into pressure, decreases by increasing the nozzle to disk spacing.

5. CONCLUSION

The flow field of a steady quasi-three-dimensional turbulent flow of a jet impinging on a rotating disk is studied numerically.

The present study showed the effect of disk rotation and centrifugal force on the radial velocity, maximum radial velocity, turbulence intensity, normal and shear components of Reynolds stress, the location of maximum radial velocity and pressure coefficient.

The major results showed that:

- The flow fields can be considered in three parts; the region with a weak effect of centrifugal force, the intermediate region and the extreme region. The influence of disk rotation appears in the intermediate region and extreme region.
- The radial velocity and the turbulence intensity increases by increasing the disk rotation in the previous zones. By increasing the distance from the nozzle to the disk, the radial velocity and the turbulence intensity decrease in the impingement zone, but increase in the wall jet.
- When the centrifugal force increases, the normal stresses and shear stresses increase.
- The spread of flow increases as the disk angular velocity decreases in the impingement zone.
- The pressure coefficient decreases as the angular velocity increases. This decay of pressure becomes bigger by increasing the nozzle to disk spacing. The numerical results give good agreement with the experiment data of Reference [15].

NOMENCLATURE

c_1, c_2, c_3, c_d	empirical constants
d	Jet diameter
H	distance between a nozzle to disk surface
k	turbulent kinetic energy
p	pressure
Re	Reynolds number ($Re = \rho V_J b/\mu$)
Re_t	turbulent Reynolds number ($Re_t = \rho V_J b/\mu_t$)
r, z	cylindrical coordinates
v'_r, v'_z, v'_θ	components of RMS turbulent fluctuation velocities
$\overline{v}'_r\overline{v}'_z, \overline{v}'_r\overline{v}'_\theta, \overline{v}'_z\overline{v}'_\theta$	shear components of Reynolds stress
V_J	average velocity at the jet inlet
V_r	radial component of local mean velocity
V_z	axial component of local mean velocity
V_θ	circumferential of local mean velocity

DOI: 10.1002/fld

Greeks letters

α	local velocity ratio ($\alpha = r^2\varpi / V_J d$)
β	parameter in RNG k–ε model, 0.012
δ	location of $V_{r\,\max}$
ε	dissipation rate of turbulent kinetic energy
η_0	parameter in RNG k–ε mode, 4.38
μ	dynamic viscosity
ρ	density
Φ	general dependent variable
σ_κ, σ_ε	model constant
ω	angular velocity desk

REFERENCES

1. Cooper D, Jackson D, Lunder B, Liao GX. Impinging jet studies for turbulence model assessment—1: flow-field experiment. *International Journal of Heat and Mass Transfer* 1993; **36**(10):2675–2684.
2. Baughn JW, Shimizu S. Heat transfer measurements from a surface with uniform heat flux and an impinging jet. *Journal of Heat Transfer* (ASME) 1989; **111**:1096–1098.
3. Lytle D, Webb B. Air jet impinging heat transfer at low nozzle plate spacing. *International Journal of Heat and Mass Transfer* 1994; **37**:1687–1697.
4. Baughn J, Hechanova A, Yan X. An experimental study of entrainment effects on the heat transfer from the flat surface to a heated circular impinging jet. *Journal of Heat Transfer* 1991; **113**:1023–1025.
5. Knowles K, Myszko M. Turbulence measurements in radial wall jets. *Experimental Thermal and Fluid Science* 1998; **17**:71–78.
6. Baydar E. Confined impinging air jet at low Reynolds numbers. *Experimental Thermal and Fluid Science* 1999; **19**:27–33.
7. Wolfshtein M. Some solutions of the plane turbulent impinging jet. *Journal of Basic Engineering*, *Transactions of the ASME* 1970; **92d**:915–922.
8. Amano Rs, Brandt H. Numerical study of turbulent axisymmetric jets impinging on a flat plate and flowing into an axisymmetric cavity. *Journal of Fluids Engineering* (ASME) 1984; **106**:410–417.
9. Poh HJ, Kumar K, Chiang HS, Mujumdar AS. Heat transfer from a laminar impinging jet of a power low fluid. *International Communications Heat Mass Transfer* 2004; **31**(2):241–249.
10. Salmanzadeh M, Mansouri SH, Farhadi M. Numerical study of flow and thermal fields in an axisymmetric turbulent jet impinging on a flat plate. *International Mechanical Engineering Conference*, Kuwait, 4–8 December 2004; 200–208.
11. Chattopadhyay H. Numerical investigation of heat transfer from impinging annular jet. *International Journal of Heat and Mass Transfer* 2004; **47**:3197–3201.
12. Brodersen S, Metzger DE, Fernando HJS. Flow generated by the impingement of a rotating surface: Part 1—basic flow patterns. *Journal of Fluids Engineering* 1996; **118**:61–67.
13. Brodersen S, Metzger DE, Fernando HJS. Flow generated by the impingement of a rotating surface: Part II—detailed flow structure and analysis. *Journal of Fluids Engineering* 1996; **118**:68–73.
14. Itoh M, Okada M. An experiment study of the radial wall jet on a rotating disk. *Experimental Thermal and Fluid Science* 1998; **17**:49–56.
15. Minagawa Y, Obi S. Development of turbulent impinging jet on a rotating disk. *International Journal of Heat and Fluid Flow* 2004; **25**:759–766.
16. Kubo L, Gouldin FC. Numerical calculations of turbulent swirling flow. *Journal of Fluids Engineering* (ASME) 1975; 310–315.
17. Yong W. *Heat Transfer and Fluid Flow in Rotating Machinery*. Springer: Berlin, 1987; 411–423.
18. Chang K-C, Chen C-S. Development of hybrid k–ε turbulence model for swirling recirculating flow under moderate to strong swirl intensities. *International Journal for Numerical Methods in Fluids* 1993; **16**:421–443.
19. Chuang S-H, Nieh T-J. Numerical simulation and analysis of three-dimensional turbulent impinging square twin-jet flow field with no-cross flow. *International Journal for Numerical Methods in Fluids* 2000; **33**:475–498.

DOI: 10.1002/fld

20. Kalita K, Dewan A, Dass AK. Predication of turbulent plane jet in cross flow. *Numerical Heat Transfer* 2002; **41**(part A):101–111.
21. Hwang C-H, Yang Y-T. Numerical simulations on the hydrodynamics of a turbulent slot jet impinging on a semi cylindrical convex surface. *Numerical Heat Transfer* 2004; **46**(Part A):995–1008.
22. El-Gabry LA, Kaminski DA. Numerical investigation of jet impingement with cross flow-comparison of Yang-Shih and standard k–ε turbulence models. *Numerical Heat Transfer* 2005; **47**(Part A):441–469.
23. Velayati E, Yoghoubi M. Numerical study of convective heat transfer from an array of parallel bluff plates. *International Journal of Heat and Fluid Flow* 2005; **26**:80–91.
24. Launder BE, Spalding DB. The numerical computation of turbulent flow. *Computer Methods in Applied Mechanics and Engineering* 1974; **3**:269–289.
25. Patankar SV. *Numerical Heat Transfer and Fluid Flow*. McGraw-Hill: New York, 1980.

DOI: 10.1002/fld